JACS Au
AN OPEN ACCESS JOURNAL OF THE AMERICAN CHEMICAL SOCIETY

pubs.acs.org/jacsau

Article

Probing Copper and Copper–Gold Alloy Surfaces with Space-Quantized Oxygen Molecular Beam

Yasutaka Tsuda,* Jessiel Siaron Gueriba, Hirokazu Ueta, Wilson Agerico Diño,* Mitsunori Kurahashi, and Michio Okada

Cite This: *JACS Au* 2022, 2, 1839–1847

Read Online

ACCESS | Metrics & More | Article Recommendations

ABSTRACT: The orientation and motion of reactants play important roles in reactions. The small rotational excitations involved render the reactants susceptible to dynamical steering, making direct comparison between experiments and theory rather challenging. Using space-quantized molecular beams, we directly probed the (polar and azimuthal) orientation dependence of O_2 chemisorption on Cu(110) and $Cu_3Au(110)$. We observed polar and azimuthal anisotropies on both surfaces. Chemisorption proceeded rather favorably with the O–O bond axis oriented parallel (vs perpendicular) to the surface and rather favorably with the O–O bond axis oriented along [001] (vs along $[\bar{1}10]$). The presence of Au hindered the surface from further oxidation, introducing a higher activation barrier to chemisorption and rendering an almost negligible azimuthal anisotropy. The presence of Au also prevented the cartwheel-like rotations of O_2.

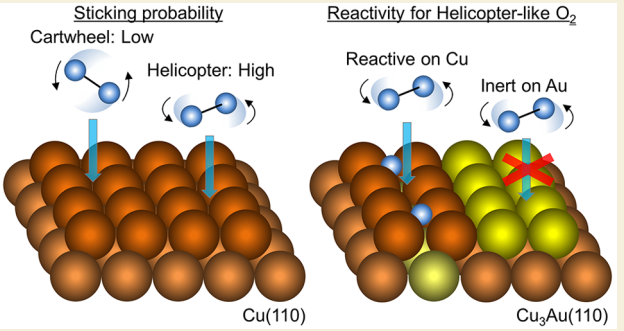

KEYWORDS: *metal surface, oxidation, copper, copper–gold alloy, steric effect*

INTRODUCTION

Activation of molecular oxygen (O_2) constitutes an important step in oxidative processes, including heterogeneous catalysis, electrocatalysis, and corrosion of metals.[1−7] The interaction of O_2 with various metal surfaces induces changes in its chemical stability and reactivity. It follows that the ability to control such processes bears on the chemical economic world. Alloying of pristine metals provides one of the simplest ways to do so. Understanding the microscopic mechanism behind O_2 chemisorption entails unraveling the stereochemistry of the processes involved.[8−14]

O_2 dissociative adsorption on Cu(110) provides a model system for understanding the oxidation processes on Cu surfaces.[15−32] The pristine Cu(110) surface possesses an anisotropic surface structure, on which anisotropic Cu–O chains grow as a precursor to oxide formation.[28−32] Early molecular beam experiments observed initial sticking probabilities (S_0) increasing with translational energy (E_t), approaching 0.8 at a high enough E_t.[24]

At low E_t, two competing mechanisms could account for the observed O_2 dissociative adsorption. A precursor-mediated channel (a weakly bound, physisorbed *trapping* molecular state) dominates at low E_t and low surface temperatures (T_S). Activated dissociative chemisorption becomes important as E_t increases, which occurs directly and/or via a *short-lived* molecularly chemisorbed state. One could also think of a *three-well* potential[33] that ascribes transient molecularly chemisorbed states to negatively ionized O_2^-, e.g., the peroxo state, as suggested by high-resolution electron energy loss spectroscopy (HREELS) measurements[17,18] and -density functional theory (DFT)-based calculations.[19] Such negatively charged states could account for the high sticking probability and the well-known efficient catalytic activity of Cu for oxidation.

At high E_t, hyperthermal molecular oxygen beam (HOMB) experiments[14] report effective formation of Cu_2O precursor on Cu(110), that exhibits dependence on the azimuthal orientation at which O_2 impinges the surface. This demonstrates another important feature that comes from the inherent orientation dependence of reactions. The stereodynamics of reactant molecules (the orientation and the movement of molecules in 3D space) plays an important role in reactions. The small rotational energy excitations involved (ca. less than a few meV) render the reactants susceptible to dynamical *steering*[1,34−36] and make direct verification of

Received: March 7, 2022
Revised: May 16, 2022
Accepted: June 7, 2022
Published: July 21, 2022

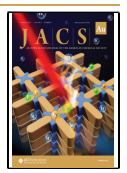

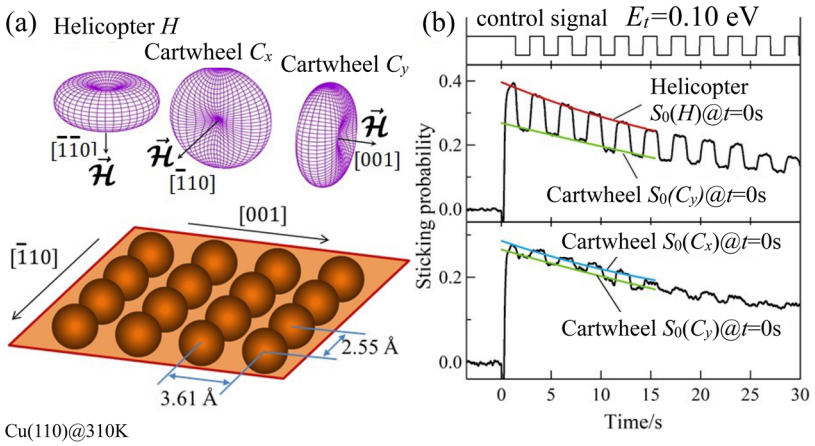

Figure 1. (Space quantized) O_2 sticking probabilities on Cu(110). (a) Angular distributions (upper panel) of the molecular axis (O−O bond axis) of an O_2 (in the triplet electronic ground state $^3\Sigma_g^-$ and spin-rotational state (J = 2, M = 2)) with respect to Cu(110) (schematically depicted in the lower panel) and corresponding defining magnetic fields $\vec{\mathcal{H}}$. Orienting $\vec{\mathcal{H}}$ perpendicular to the surface, i.e., along [$\bar{1}$ $\bar{1}$0], results in helicopter-like rotating O_2. Two types of cartwheel-like rotating O_2 can also be realized by orientating $\vec{\mathcal{H}}$ parallel to the surface, i.e., either along [$\bar{1}$10] or [001]. (b) Time evolution of the sticking probability for a space-quantized O_2 impinging on Cu(110) (at a surface temperature of ca. 310 K) with translational energy E_t = 0.10 eV. Time t = 0 corresponds to the time the beam shutter is opened to allow the molecular beam to impinge on the surface. Following the control signal shown (topmost right panel), the $\vec{\mathcal{H}}$ direction can be modulated to alternately produce helicopter-like (high signal) and cartwheel-like (low signal) rotating O_2 that impinge on Cu(110). Numerical fits to the corresponding sticking probability data points (using exponentially decaying functions extrapolated to t = 0) also shown to guide the eye. The values at t = 0 correspond to the initial sticking probabilities $S_0(H)$, $S_0(C_x)$, and $S_0(C_y)$.

calculated potential energy surfaces (PES) rather challenging.[1,10−14,25,37] Helicopter-like rotating O_2 (with dominant rotational angular momentum **J** parallel along the surface normal) adsorbs more effectively than cartwheel-like rotating O_2 (with **J** perpendicular to the surface normal).[19,20,22] As mentioned earlier, a possible candidate for transient molecularly chemisorbed state would be an adsorbed O_2 exhibiting peroxo-like character (O_2^-), with azimuthal orientation-dependent stability.[19,20,22] As expected from previous discussions,[34−36] at high E_t (ca. 500 meV), the impinging O_2 does not have enough time to reorient (be steered) and the favorable helicopter-like rotating O_2 dominantly account for chemisorption.[19] On the other hand, at low E_t (ca. 50 meV), the impinging O_2 have enough time to reorient (be steered) to more favorable orientations toward reactive sites.[19]

Ancient people know that alloying with inert gold (Au) protects Cu from further corrosion, and we observe several ancient products enduring in rather pristine condition.[38] Now, we know that the deeper *d*-band center induced by Au alloying prevents the strong bonding−antibonding interaction with the antibonding state of the impinging O_2, resulting in the inertness of the alloy surface.[33,39,40] Moreover, the presence of Au changes the electron distribution (electronic corrugation) on the Cu surface. Thus, one would expect different dynamical processes (e.g., translational to rotational energy transfer effects) occurring when O_2 impinges on a Cu−Au alloy surface as compared to a Cu surface.

In this study, we clarify the alignment dependence of O_2 chemisorption on Cu(110) and Cu_3Au(110). We do this by using a single-quantum-state-selected (space quantized, following the 1922 Stern-Gerlach experiment[41,42]) O_2 beam developed at NIMS (for which both the molecular alignment and the spin state are well-defined).[10] On Cu(110), as in previous studies, we observed both polar and azimuthal anisotropies. O_2 chemisorption proceeds rather favorably with the O−O bond axis oriented parallel (vs perpendicular) to the surface and rather favorably with the O−O bond axis oriented along [001] (vs along [$\bar{1}$10]). O_2 chemisorption on Cu_3Au(110) shows similar polar and azimuthal anisotropies. However, the presence of Au hinders the surface from further oxidation via a higher activation barrier to chemisorption and an almost negligible azimuthal anisotropy.

RESULTS AND DISCUSSION

In Figure 1, we show the measured alignment-dependent O_2 initial sticking probabilities (S_0) on Cu(110). O_2 in a spin rotational state [(J, M) = (2,2)] exhibit a $\sin^2\theta$-dependent O−O bond axis (angular) distribution, where θ gives the polar angle subtended by the O−O bond axis with a predetermined defining magnetic field ($\vec{\mathcal{H}}$). Thus, helicopter-like and cartwheel-like rotating O_2 (vide ante) can be generated, achieved by directing $\vec{\mathcal{H}}$ perpendicular or parallel to the surface (Figure 1a). Helicopter-like rotating O_2 have O−O bond axes oriented dominantly parallel to the surface. On the other hand, for cartwheel-like rotating O_2, the O−O bond axes can assume both parallel and perpendicular configurations. We can further prepare two types of cartwheel-like rotating O_2 depending on their azimuthal orientation, e.g., by aligning $\vec{\mathcal{H}}$ along [$\bar{1}$10] (Cartwheel (x), C_x) or along [001] (Cartwheel (y), C_y) (see Figure 1a).

In Figure 1b, we show the time evolution of the sticking probability for O_2 on Cu(110), measured while modulating $\vec{\mathcal{H}}$ to alternately produce helicopter-like and cartwheel-like O_2 at E_0 = 0.10 eV. We determined the sticking probability curves by fitting the data points corresponding to each geometry to an exponential decay function (see smooth curves), and the values extrapolated to t = 0 (beam shutter removed) correspond to initial sticking probabilities $S_0(H)$ and $S_0(C_y)$, respectively. Because we are discussing the very early stage of oxidation, Cu segregation[40,43,44] induced by oxygen adsorption need not be considered in S_0. We see that $S_0(H)$ > $S_0(C_y)$ and $S_0(H)$ >

https://doi.org/10.1021/jacsau.2c00156
JACS Au 2022, 2, 1839−1847

$S_0(C_x)$, in general, indicating that more reactive parallel-oriented O_2 as compared to perpendicular-oriented O_2. This is consistent with previous XPS studies on Cu(111).[45]) From Figure 1b, we can also see from the time evolution of the sticking probabilities that $S_0(C_x) > S_0(C_y)$, indicating that O_2 with O−O bond axes oriented along [001] are more reactive than those with O−O bond axes oriented [$\bar{1}$10].

In Figure 2, we show the corresponding results on $Cu_3Au(110)$-(4 × 1). Low-energy electron diffraction

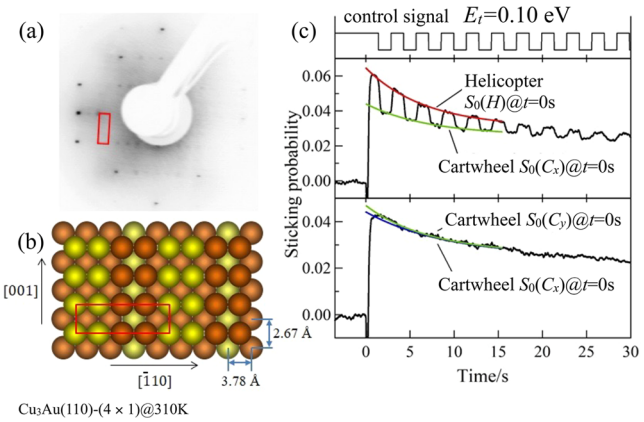

Figure 2. (Space quantized) O_2 sticking probabilities on Cu_3Au-(110)-(4 × 1). (a) LEED patterns for a clean $Cu_3Au(110)$-(4 × 1). (b) Schematic depiction of $Cu_3Au(110)$-(4 × 1) (Cu, reddish balls; Au, yellowish balls). (c) Time evolution of the sticking probability for a space-quantized O_2 impinging on $Cu_3Au(110)$-(4 × 1) (at a surface temperature of ca. 310 K) with translational energy E_t = 0.10 eV. Time t = 0 corresponds to the time the beam shutter is opened to allow the molecular beam to impinge on the surface. Following the control signal shown (topmost right panel), the direction of the defining magnetic field $\vec{\mathcal{H}}$ can be modulated to alternately produce helicopter-like (high signal) and cartwheel-like (low signal) rotating O_2 that impinge on $Cu_3Au(110)$-(4 × 1). Numerical fits to the corresponding sticking probability data points (using exponentially decaying functions extrapolated to t = 0) also shown to guide the eye. The values at t = 0 correspond to the initial sticking probabilities $S_0(H)$, $S_0(C_x)$, and $S_0(C_y)$.

(LEED) patterns (Figure 2a) indicate Au atom segregation, forming a (4 × 1) restructured surface[46] (see Figure 2b). A detailed layer profile of the surface analyses[43] found that 50% of surface Cu atoms on Cu(110) were replaced by Au atoms. This results in a reduction in the O_2 sticking probability to 15% of that on Cu(110). The reduced sticking probability indicates effects from the second-layer Au atoms and/or the nonlocalized contribution of the first-layer Au atoms to the reactive sites. Although we expect the existence of transient molecular states similar to that on Cu(110), the deeper d-states of Au interact weakly with the antibonding states of O_2 without filling them with electrons, rendering it more difficult to form intermediate $O_2^{\delta-}$ states. Moreover, the expected larger work function of $Cu_3Au(110)$ compared to Cu(110) (ca. 4.48 eV, and ca. 5.37 eV for Au(110))[47,48] renders negatively charged states unstable. As on Cu(110), we see that $S_0(H) > S_0(C_y)$ and $S_0(H) > S_0(C_x)$, in general. Again, this indicates more reactive parallel-oriented O_2 as compared to perpendicular-oriented O_2. However, in contrast to the case on Cu(110), we find negligible azimuthal anisotropy on $Cu_3Au(110)$-(4 × 1), as now we have $S_0(C_x) \sim S_0(C_y)$.

To determine how the translational/beam energy E_t affects the steric effect, in Figure 3a, we plot the ratios $S_0(H)/S_0(C_x)$

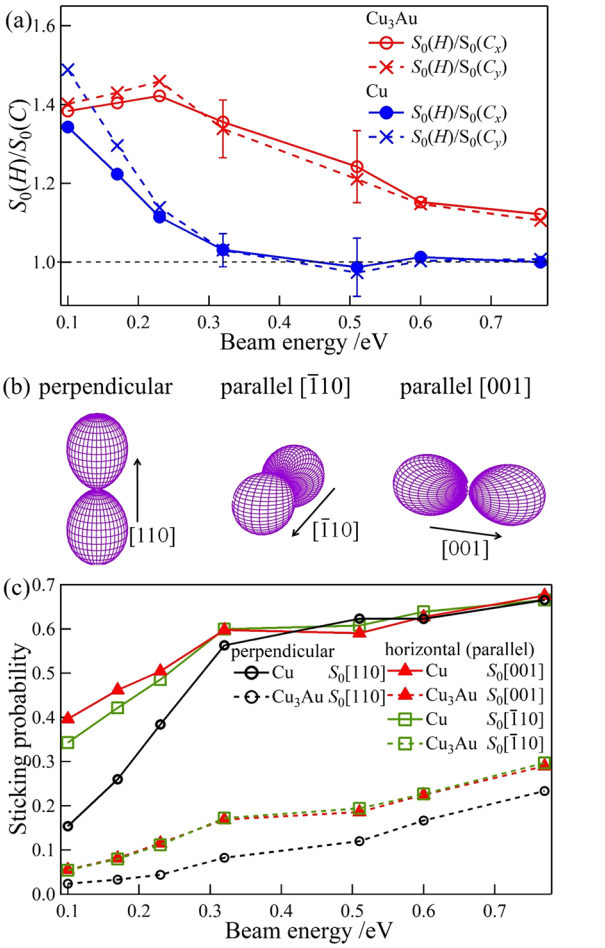

Figure 3. Translational energy dependence of (space quantized) O_2 initial sticking probabilities on Cu(110) and $Cu_3Au(110)$. (a) Initial sticking probability ratio $S_0(H)/S_0(C)$ for helicopter-like and cartwheel-like rotating O_2 on Cu(110) and $Cu_3Au(110)$ at 310 K. (b) Angular distributions of the O_2 molecular axis (O−O bond axis) oriented perpendicular (along [110]) and parallel (along [$\bar{1}$10] and [001]) to the corresponding surfaces. (c) Initial sticking probability contributions from the O−O bond axis oriented perpendicular and parallel to Cu(110) and $Cu_3Au(110)$ as indicated in panel b.

and $S_0(H)/S_0(C_y)$, determined from $S_0(H)$ and $S_0(C)$ obtained simultaneously by a single modulation measurement, as a function of E_t. Theoretically, when O_2 with O−O bond axes oriented parallel the surface adsorb, we have $S_0(H)/S_0(C_x) = 2$ (or $S_0(H)/S_0(C_y) = 2$). And when O_2 can adsorb regardless of O−O bond axes orientations, we have $S_0(H)/S_0(C_x) = 1$ (or $S_0(H)/S_0(C_y) = 1$). Experimentally, on Cu(110), we find $S_0(H)/S_0(C_x) = 1.35$ and $S_0(H)/S_0(C_y) = 1.5$ at E_t = 0.10 eV, and $S_0(H)/S_0(C_x) \sim S_0(H)/S_0(C_y) \sim 1.0$ for $E_t \geq 0.33$ eV. This indicates the importance of steric effects at small E_t, becoming negligible for translational/beam energies $E_t \geq 0.33$ eV. On $Cu_3Au(110)$-(4 × 1), the E_t-dependence of $S(H)/S(C)$ follows a trend similar to that observed on Pt(111),[49] i.e., initial increase in $S_0(H)/S_0(C_x)$ and $S_0(H)/S_0(C_y)$ at $E_t \leq 0.26$ eV, and then a gradual decrease from $E_0 \geq 0.26$ eV.

To determine how the O−O bond axes orientation with respect to the surface normal affects the sticking probability on Cu(110) and $Cu_3Au(110)$, we plot in Figure 3c the E_t-

https://doi.org/10.1021/jacsau.2c00156
JACS Au 2022, 2, 1839−1847

dependent orientation-resolved sticking probabilities $S_0[001]$ and $S_0[\bar{1}10]$ for O_2 with O−O bond axes oriented parallel to the surface (along [001] and $[\bar{1}10]$, respectively) and $S_0[110]$ for O_2 with O−O bond axes oriented perpendicular to the surface (along [110]). (For details on how to determine the orientation resolved sticking probabilities, we refer the readers to the Experimental and Theoretical Methods.)

On Cu(110), $S_0[110]$, $S_0[\bar{1}10]$, and $S_0[001]$ all increase gradually with increasing E_t (see Figure 3c). Again, we observe an orientational dependence favoring O−O bond axes oriented parallel to the surface (see $S_0[\bar{1}10] > S_0[110]$ and $S_0[001] > S_0[110]$ for Cu(110) in Figure 3c). We also observe an in-plane azimuthal orientation dependence favoring O−O bond axes oriented parallel to the surface along [001] (see $S_0[001] > S_0[\bar{1}10]$ for Cu(110) in Figure 3c). And, as we have observed earlier, we also see that both polar and azimuthal orientational dependence becomes negligible at $E_t > 0.3$ eV.

On $Cu_3Au(110)$-(4 × 1), we also see that $S_0[110]$, $S_0[\bar{1}10]$, and $S_0[001]$ all increase gradually with increasing incident translational (beam) energy (see Figure 3c). Again, we observe an orientational dependence favoring O−O bond axes oriented parallel to the surface (see $S_0[\bar{1}10] > S_0[110]$ and $S_0[001] > S_0[110]$ for $Cu_3Au(110)$-(4 × 1) in Figure 3c), which persists throughout the incident translational (beam) energy range of the experiment, i.e., E_t[eV]: [0.1, 0.8]. And, as we have observed earlier, we find negligible in-plane azimuthal orientation dependence.

Upon further examination of the ratios of the corresponding initial sticking probabilities (see Figure 6), we see that the presence of Au considerably decreases the adsorption of O_2 with O−O bond axes oriented perpendicular to the surface (i.e., O−O bond axes parallel to [110]). We also see a negligible effect on the adsorption of O_2 with O−O bond axes oriented parallel to the surface (i.e., O−O bond axes parallel to [001] and $[\bar{1}10]$).

In the following, we discuss the origin of the different energy dependence of S_0 and its steric effects for Cu(110) and $Cu_3Au(110)$. As has been shown in the previous study on Cu(110),[24] a barrier exists before O_2 enters the chemisorption well of $O_2^{\delta-}$. The magnitude of the barrier depends on the angle of O_2 axis relative to the surface plane and on the impact position in the surface unit cell. Molecularly adsorbed O_2 is stable in the geometry with its molecular axis parallel to the surface.[16,19,20] Thus, it is reasonable to expect that the activation barrier to the $O_2^{\delta-}$ state is lower if O_2 approaches with its molecular axis parallel to the surface. We show that the potential energy curves (PEC) of O_2 on Cu(110) manifest such preference (see Figure 4). Moreover, the preferential orientation of O_2^{2-} is parallel to the [001] direction.[19,20] Therefore, the azimuthal dependence of S_0 appeared at $E_t \lesssim 0.20$ eV, possibly revealing the azimuthal dependence of $O_2^{\delta-}$ stability. Considering bond dissociation, we also plot the potential energy surface (PES) for O_2 in Figure 5. Here, the collisions on the on-top site and the bridge site are not considered because the high activation barrier of such sites cannot be overcome at the experimental incident energy. The adsorption energies of O_2 on Cu(110), at [001] and $[\bar{1}10]$ bond orientations, are −1.82 and −1.66 eV, respectively. Moreover, the activation barrier appears in the entrance channel. By tracing the minimum energy path, we found a relatively higher energy barrier for O_2 dissociation at the $[\bar{1}10]$ orientation than at the [001] bond orientation on Cu(110). The energy difference between the barriers is about 40 meV.

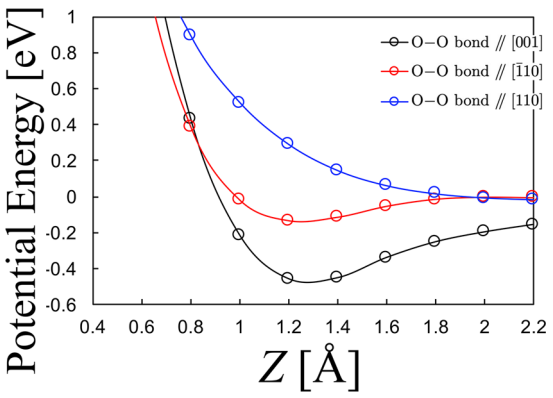

Figure 4. Orientation dependent potential energy curves (PECs) for O_2/Cu(110). PECs shown as a function of the O_2 center-of-mass distance Z (Å) above a 4-fold hollow site on Cu(110). PECs calculated with the O−O bond length fixed at a gas phase equilibrium distance of 1.23 Å, and the O−O bond axis orientations fixed parallel to $[\bar{1}10]$, [001], and [110] on Cu(110). Energies (eV) given with respect to O_2 sufficiently far (ca. 5.0 Å) from Cu(110). Structures and related figures drawn using the *VESTA* package.[66]

These comparative results agree well with previous calculations on Cu(110).[18,19] S_0 increasing with increasing E_t can be explained by the widened range of impact parameters at which incident O_2 molecules surmount the barrier. At $E_t \geq 0.33$ eV, $S_0(H)/S_0(C) \sim 1.0$ and sticking probability saturates at ∼0.65. The lower saturation of sticking probability compared to the previously reported value ∼0.8[23] may be caused by the single rotational state in the beam. On the other hand, the continued S_0 increase upon increasing E_t could be expected because incident O_2 molecules surmount the higher barrier at the bridge and/or on-top sites, but the saturation of S_0 is different from such expectation. Moreover, $S_0(H)/S_0(C) \sim 1.0$ at $E_t \geq 0.33$ eV indicates no steric preference in O_2 sticking. However, the potential landscape and the corresponding energy dissipation process is expected to be quite different for both geometries. To explain the difference between the results and expectation, we speculate the following. The experimental result of $S_0(H)/S_0(C) \sim 1.0$ suggests the contribution of charge transfer[50,51] into $O_2^{\delta-}$ state after overcoming the activation barrier at $E_t \geq \sim 0.4$ eV.[51] The high-energy O_2 comes over the seam between the physisorption state and molecularly adsorbed state. Charge transfer occurs, the short-lived excited $O_2^{\delta-}$ state couples with substrate excitations, and then de-excited, trapped, and finally O_2 dissociates. Although the ground-state interaction potential of $O_2^{\delta-}$ depends on the alignment of the molecular axis against the surface, the trapping process into the excited $O_2^{\delta-}$ state may not strongly depend on the molecular orientation of O_2 because various excited states coupling with the surface are available after the first activation seam into the molecularly adsorbed state is overcome. The steering effects after overcoming the activation barrier also smear out the orientation dependence of charge transfer. The saturation of the sticking probability suggests that the impact condition (location of O_2 and the reaction site at the surface) at which the $O_2^{\delta-}$ state is stable enough for the dissociative adsorption is limited.

$Cu_3Au(110)$ has a work function larger than Cu(110).[47] We can thus expect a rather correspondingly less stable $O_2^{\delta-}$ state. This renders it more difficult for charge transfers to occur, requiring higher E_t as compared to that on Cu(110). Note that there are more stable molecularly chemisorbed O_2 states on Cu

https://doi.org/10.1021/jacsau.2c00156
JACS Au 2022, 2, 1839−1847

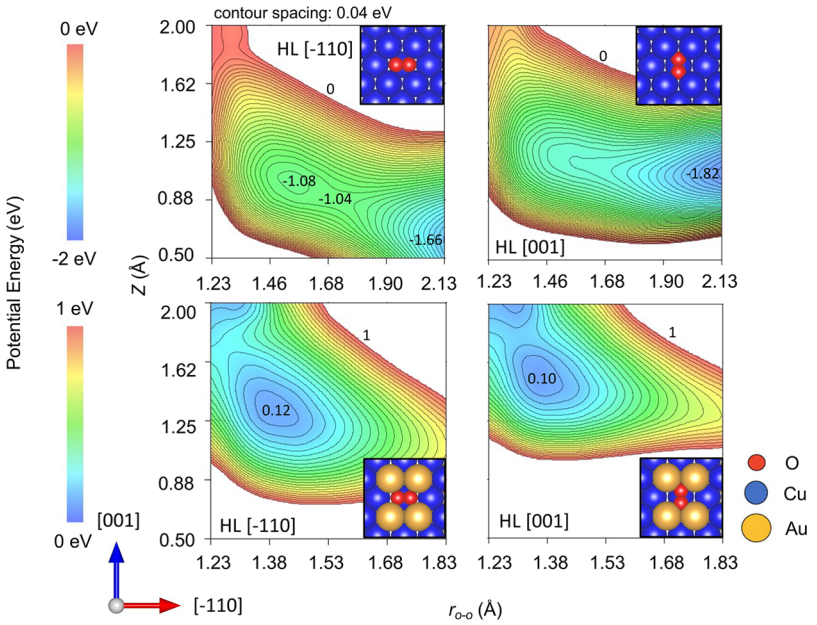

Figure 5. Potential energy surfaces (PESs) for O_2 on Cu(110) and $Cu_3Au(110)$-(4 × 1). Potential energy surfaces (PESs) for O_2 and $Cu_3Au(110)$-(4 × 1). PESs shown as functions of the O_2 center-of-mass distance Z (Å) (from the 4-fold hollow site (HL) of Cu on Cu(110) (upper panels) and Au on $Cu_3Au(110)$-(4 × 1) (lower panels)) and the O_2 bond length r_{O-O} (Å). PESs calculated with the O_2 bond axis fixed either parallel to $[\bar{1}10]$ (left panels) or parallel to [001] (right panels). Energies (eV) given with respect to O_2 sufficiently far (ca. 5.0 Å) from the surface, in increments of ca. 0.04 eV.

than on Au.[1] Consistent with that, Figure 5 shows an endothermic molecularly adsorbed $O_2^{\delta-}$ state, with adsorption energies of 0.10 and 0.12 eV, respectively. The ground state O_2 becomes unstable (ca. > 1 eV) by Au alloying.

The increase in $S_0(H)/S_0(C)$ at $E_t \lesssim 0.26$ eV on $Cu_3Au(110)$ can be accounted for by the decreasing contribution of the trapping-mediated process in the physisorption well with increasing E_t. This means that the value of $S_0(H)/S_0(C)$ for the directly activated process would be higher than the observed value and be close to 2, suggesting that for the direct process to occur at low E_t conditions, the O−O bond axes must be parallel to the surface. The azimuthal dependence observed on Cu(110) disappears on $Cu_3Au(110)$ because of the absence of a stable $O_2^{\delta-}$ state (see Figure 5). Note that the stability of the $O_2^{\delta-}$ depends on its azimuthal orientation on $Cu_3Au(110)$, and also susceptible to ensemble effect of interaction potentials. The 3% larger lattice constant of Cu_3Au than Cu renders the active sites for the dissociation of the horizontal molecules practically azimuthally isotropic. The steering effect, which redirects the impinging O_2 to the preferred geometry becomes insufficient at high energies, e.g., E_t > 0.26 eV. At higher E_t, O_2 with O−O bond axes oriented perpendicular to the surface can also overcome the activation barrier. The angular distribution of the O−O bond axes could also smear out the steric effect, with the reaction occurring at a finite range of orientations depending on E_t.

In Figure 6, we show the translational energy dependence of the initial sticking probability ratios $S_0(Cu_3Au)/S_0(Cu)$ for $S_0[001]$, $S_0[\bar{1}10]$, and $S_0[110]$. $S_0(Cu_3Au)/S_0(Cu)$ for $S_0[110]$ exhibits the least value compared to the rest and indicates that Au alloying effectively reduces the sticking of O_2 with O−O bond axes oriented perpendicular to the surface. Au alloying filters the molecular orientation and permeates only O_2 with O−O bond axes oriented horizontal to the surface and supply the O atoms. This filtering effect may lead to the selective

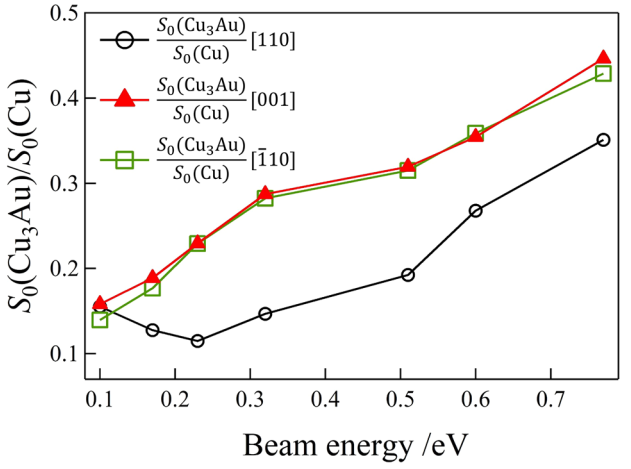

Figure 6. Ratios of (space quantized) O_2 initial sticking probabilities on Cu(110) and $Cu_3Au(110)$. Initial sticking probability ratios for O_2 adsorption on $Cu_3Au(110)$-(4 × 1) and Cu(110), with the O−O bond axis oriented along [110], [001], and $[\bar{1}10]$ ($S_0(Cu_3Au)/S_0(Cu)[110]$, $S_0(Cu_3Au)/S_0(Cu)[001]$, and $S_0(Cu_3Au)/S_0(Cu)$-$[\bar{1}10]$, respectively).

surface chemical reactions and selective oxidative catalytic reactions. Reduction in corrosion of Au alloyed Cu may be attributed to the reduction in the presence (if not complete absence) of intermediate *short-lived* $O_2^{\delta-}$ that increases reactivity but reduces the steric preference in processes at higher E_t.

Charge population analyses of adsorbed O_2 on $Cu_3Au(110)$ and Cu(110) indicate electron gain ($O_2^{\delta-}$ states, see Table 1). Hence, a shallow potential for molecularly chemisorbed O_2 on Cu_3Au suggests that dissociation via the transiently trapped $O_2^{\delta-}$ will be difficult, and the dissociative adsorption may occur over the high adiabatic activation barrier in the

https://doi.org/10.1021/jacsau.2c00156
JACS Au 2022, 2, 1839−1847

Table 1. Electron Gain (*e*-Gain) of O_2 Adsorbed on $Cu_3Au(110)$-(4 × 1) and Cu(110)[a]

surface	O−O bond axis orientated along	O−O bond length (Å)	*e*-gain (*e*)
$Cu_3Au(110)-(4\times1)$	[001]	1.33	0.61
$Cu_3Au(110)-(4\times1)$	[$\bar{1}$10]	1.43	0.78
Cu(110)	[001]	2.13	1.58
Cu(110)	[$\bar{1}$10]	2.13	1.72

[a] *e*-gain (*e*) given with respect to O_2 sufficiently far (ca. 5.0 Å) from the corresponding surfaces.

(approximately) usual two-well potential. Unstable molecular chemisorbed O_2 states on Cu_3Au results in weakened orientation dependence of the O_2 sticking probability. In addition, the large atomic radii of surface Au atoms lessen the anisotropy of the surface charge distribution on $Cu_3Au(110)$ (see Figure 7). Correspondingly, the electron surface corrugation as seen by an impinging O_2 on Cu(110) varies more between [001] and [$\bar{1}$10] bond orientations, having a relatively smooth electron surface distribution along the [$\bar{1}$10] direction or the [001] plane. Collectively, these results confirm the azimuthal dependence of O_2 adsorption on Cu(110) and its inertness toward $Cu_3Au(110)$.

CONCLUSION

In conclusion, we demonstrate the effect of alloying on the steric effects in O_2 dissociative adsorption. At low beam energies, the dissociative adsorption of O_2 occurs on the adiabatic potential landscape on Cu(110). O_2 with O−O bond axes parallel to the surface exhibit higher reactivity as compared to those oriented normal to the surface. The reactivity also depends on the O−O bond orientations along the surface. At high beam energies, the O_2 in all orientations overcome the activation barrier and steric effects become negligible. Reactions via charge transfer into *short-lived* $O_2^{\delta-}$ state also smear out the steric effects and reduce initial sticking probability saturations to ca. 0.7. On $Cu_3Au(110)$, the overall initial sticking probabilities reduce to ca. 15% that of on Cu(110). Except for the negligible azimuthal orientation dependence, the reactivity also shows similar dependence on the O−O bond axes orientations with respect to the surface, as on Cu(110). Alloying with Au increases the activation barrier in the entrance channel, increases the work function, and renders the molecularly chemisorbed O_2 ($O_2^{\delta-}$) state unstable.

EXPERIMENTAL AND THEORETICAL METHODS

Sample Preparation

We cleaned the Cu(110) and $Cu_3Au(110)$ samples by 1.0 eV Ar^+ sputtering and annealing at 773 K. We repeated this procedure until we could no longer detect the impurities by Auger electron spectroscopy (AES).

Space-Quantized, State-Selected $O_2(^3\Sigma^-_g)$ Molecular Beam

For details regarding the experimental apparatus, we refer the readers to previous reports.[10,13] Briefly, we generated O_2 molecular beams by the free expansion of seeded gas of O_2/He. We then used hexapole magnets to filter the (J, M) state from the O_2 molecular beam. We could also control the translational energy of the state-selected O_2(J, M) beam by adjusting the number of the hexapole magnets and the O_2/He mixing ratio of the seeded O_2 beam. Note that we use the following notations:

J = **K** + **S**: O_2 total angular momentum with corresponding quantum number J;

K: O_2 rotational angular momentum with corresponding quantum number K;

S: O_2 total electron spin angular momentum with corresponding quantum number S;

$M = M_K + M_S$: projection of **J** along the external field direction;

M_K and M_S: projection of **K** and **S** along the external field direction, respectively;

Thus, we are able to prepare $O_2(J = 2, M = 2)$, which corresponds to $O_2(K = 1, M_K = 1, S = 1)$, with rotational energy $E_K = BK(K + 1) \approx (0.18\ \text{meV})(1)(1 + 1) = 0.36$ meV, and translational energy E_t. An O_2 in state ($K = 1$, $E_t = 100$ meV) would have traveled a distance of 15 Å by the time it rotates 90°.

The angular distribution of the $O_2(J = 2, M = 2)$ molecular axis orientation approximately follows a $\sin^2\theta$ distribution, where θ is the polar angle of the O_2 molecular axis relative to the direction of the defining magnetic field $\vec{\mathcal{H}}$. Depending on the orientation of the defining magnetic field $\vec{\mathcal{H}}$, i.e., perpendicular or parallel to the surface, we could have helicopter- or cartwheel-like rotating $O_2(J = 2, M = 2)$. Helicopter-like rotating $O_2(J = 2, M = 2)$ have an O−O bond axis oriented parallel to the surface. Cartwheel-like rotating $O_2(J = 2, M = 2)$ can also have O−O bond axis orientations other than parallel to the surface (i.e., perpendicular and in between). By aligning $\vec{\mathcal{H}}$

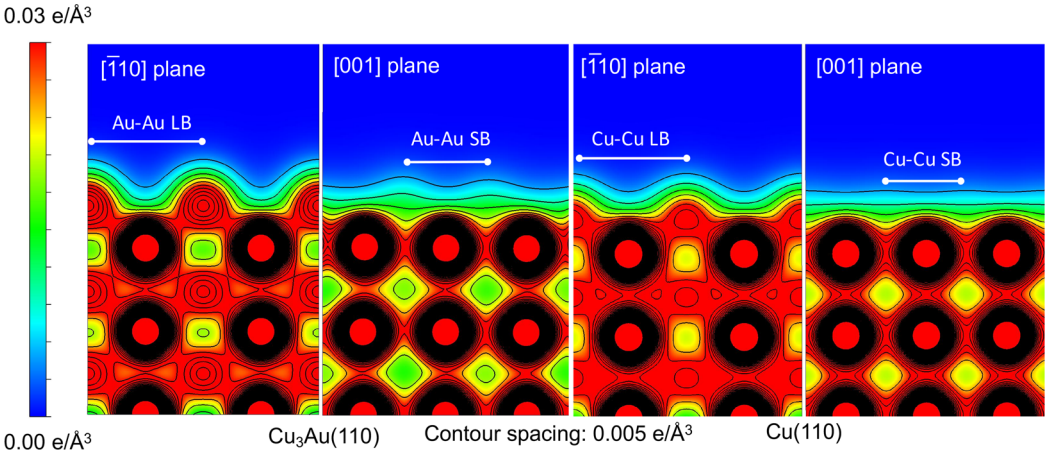

Figure 7. Electron distribution on $Cu_3Au(110)$ and Cu(110). 2D cut through the long bridge (LB) and short bridge (SB) sites of the electron distributions as viewed along [$\bar{1}$10] and [001] on the corresponding surfaces. Note the more pronounced orientation-dependent contour difference observed on Cu(110) than on $Cu_3Au(110)$-(4 × 1). Electron distributions (e/Å^3) given with respect to distances sufficiently far (ca. 5.0 Å) from the surface, in increments of 0.005 e/Å^3.

https://doi.org/10.1021/jacsau.2c00156
JACS Au 2022, 2, 1839−1847

parallel to [$\bar{1}$10] or [001], we can prepare two types of cartwheel-like rotating O_2, which we label as cartwheels C_x and C_y, respectively. Thus, we can prepare a space-quantized, state-selected $O_2(^3\Sigma^-_g)$ molecular beam, in which nearly all (ca. 100%) of the molecules are in the spin-rotational state (J = 2, M = 2).

Initial Sticking Probabilities for Helicopter-like and Cartwheel-like Rotating $O_2(J = 2, M = 2)$

We express the initial sticking probability $S_0(H)$ for helicopter-like rotating $O_2(J = 2, M = 2)$ as[10]

$$S_0(H) = \frac{3}{4\pi}\int_0^{2\pi} d\phi \int_0^{\pi/2} R_{ave}(\theta, \phi)\sin^3\theta d\theta \quad (1)$$

For the two types of cartwheel-like rotating $O_2(J = 2, M = 2)$, viz., $S_0(C_x)$ and $S_0(C_y)$, we have

$$S_0(C_x) = \frac{3}{4\pi}\int_0^{2\pi} d\phi \int_0^{\pi/2} R_{ave}(\theta, \phi)(1 - \sin^2\theta\sin^2\phi)\sin\theta d\theta \quad (2)$$

and

$$S_0(C_y) = \frac{3}{4\pi}\int_0^{2\pi} d\phi \int_0^{\pi/2} R_{ave}(\theta, \phi)(1 - \sin^2\theta\cos^2\phi)\sin\theta d\theta \quad (3)$$

(θ, ϕ) give the polar and azimuthal orientation of the O_2 molecular axis with respect to the surface. $R_{ave}(\theta, \phi)$ gives the reaction rate averaged over the surface unit cell. From eqs 1−3, we then determine the initial sticking probability $S_0(R)$ for a random distribution, i.e.,

$$S_0(R) = \frac{1}{3}S_0(H) + \frac{1}{3}S_0(C_x) + \frac{1}{3}S_0(C_y) = \frac{1}{4\pi}\int_0^{2\pi} d\phi \int_0^{\pi/2} R_{ave}(\theta, \phi)\sin\theta d\theta \quad (4)$$

For initial sticking probabilities S_0[110], S_0[001], and S_0[$\bar{1}$10], which correspond to O_2 with molecular axis parallel to [110], [001], and [$\bar{1}$10], respectively, we have

$$S_0[110] = -S_0(H) + S_0(C_x) + S_0(C_y) = \frac{3}{4\pi}\int_0^{2\pi} d\phi \int_0^{\pi/2} R_{ave}\cos^2\theta\sin\theta d\theta \quad (5)$$

$$S_0[001] = S_0(H) + S_0(C_x) - S_0(C_y) = \frac{3}{4\pi}\int_0^{2\pi} d\phi \int_0^{\pi/2} R_{ave}\sin^3\theta\sin^2\phi d\theta \quad (6)$$

$$S_0[\bar{1}10] = S_0(H) - S_0(C_x) + S_0(C_y) = \frac{3}{4\pi}\int_0^{2\pi} d\phi \int_0^{\pi/2} R_{ave}\sin^3\theta\cos^2\phi d\theta \quad (7)$$

Computational Details

We performed spin-polarized density functional theory[52,53] (DFT) based total energy calculations,[54−57] using the projector augmented wave (PAW) formalism.[58] We employed plane wave basis set, with a cutoff energy of 700 eV. We used the Perdew−Burke−Ernzerhof (PBE) generalized gradient approximation (GGA) for the exchange correlation functional.[59,60] We adopt the Monkhorst and Pack method to perform Brillouin zone integrations, with 10 × 10 × 1 special k-points,[61] and conduct frozen lattice calculations with energy convergence of less than 1 × 10^{-5} eV. To model the Cu(110) and Cu_3Au(110), we used a periodic slab, six atomic layers thick with eight atoms per layer, separated by 15 Å of vacuum along [110]. To obtain the optimized geometry after surface cleaving, we relaxed the first 2 atomic layers of the surface slabs until Hellmann−Feynman forces are less than 0.01 eV/Å. We used a (4 × 2) surface unit cell of Cu(110) and Cu_3Au(110) as the supercell for O_2 adsorption. This takes care of the unwanted interaction between periodic images of O_2. In the case of Cu_3Au(111), we adopt the (4 × 1) reconstructed structure for the first two atomic layers. To have a better comparison of the relative strength of adsorption on Au surface atoms of Cu_3Au(110) and on Cu surface atoms of pristine Cu(110), we chose the 4-fold coordinated Au/Cu hollow site as O_2 adsorption site. We determined the adsorption energies from the change in the total energy of the system with respect to the case with O_2 sufficiently far (ca. 5 Å) from the surface. To determine the charge population of O_2 upon adsorption, we used Bader charge analyses.[62−65] We used the *VESTA* package[66] to draw the structures and related figures.

AUTHOR INFORMATION

Corresponding Authors

Yasutaka Tsuda − *Department of Chemistry, Osaka University, Toyonaka, Osaka 560-0043, Japan; Materials Sciences Research Center, Japan Atomic Energy Agency, Sayo-gun, Hyogo 679-5148, Japan;* orcid.org/0000-0003-4992-6237; Email: tsuda.yasutaka@jaea.go.jp

Wilson Agerico Diño − *Department of Applied Physics and Center for Atomic and Molecular Technologies, Osaka University, Suita, Osaka 565-0871, Japan;* orcid.org/0000-0001-6154-7681; Email: wilson@dyn.ap.eng.osaka-u.ac.jp

Authors

Jessiel Siaron Gueriba − *Department of Applied Physics, Osaka University, Suita, Osaka 565-0871, Japan;* Present Address: Institute of Laser Engineering, Osaka University, Suita, Osaka 565−0871, Japan

Hirokazu Ueta − *National Institute for Materials Science, Tsukuba, Ibaraki 305-0047, Japan;* Present Address: Advanced Science Research Center, Japan Atomic Energy Agency, Tokai, Ibaraki 319−1195, Japan; orcid.org/0000-0003-3026-101X

Mitsunori Kurahashi − *National Institute for Materials Science, Tsukuba, Ibaraki 305-0047, Japan;* orcid.org/0000-0002-3802-4513

Michio Okada − *Department of Chemistry and Institute for Radiation Sciences, Osaka University, Toyonaka, Osaka 560-0043, Japan;* orcid.org/0000-0002-7689-4288

Complete contact information is available at: https://pubs.acs.org/10.1021/jacsau.2c00156

Notes

The authors declare no competing financial interest.

ACKNOWLEDGMENTS

We thank MEXT (Ministry of Education, Culture, Sports, Science and Technology-Japan) for Grants-in-Aid for Scientific Research (JP20H02623, JP20K21148, JP20K21171, JP15KT0062, JP26248006, JP20H02638) and the NIMS Joint Research Hub Program. Structures and related figures appearing in the manuscript were drawn using the *VESTA* package.[66]

REFERENCES

(1) Montemore, M. M.; van Spronsen, M. A.; Madix, R. J.; Friend, C. M. O. O_2 activation by metal surfaces: implications for bonding and reactivity on heterogeneous catalysts. *Chem. Rev.* **2018**, *118*, 2816−2862.

(2) Huang, W.; Sun, G.; Cao, T. Surface Chemistry of group IB metals and related oxides. *Chem. Soc. Rev.* **2017**, *46*, 1977−2000.

(3) Stampfl, C.; Soon, A.; Piccinin, S.; Shi, H.; Zhang, H. Bridging the temperature and pressure gaps: close-packed transition metal

https://doi.org/10.1021/jacsau.2c00156
JACS Au 2022, 2, 1839−1847

surfaces in an oxygen environment. *J. Phys.: Condens. Matter* **2008**, *20*, 184021.
(4) Lundgren, E.; Mikkelsen, A.; Andersen, J. N.; Kresse, G.; Schmid, M.; Varga, P. Surface oxides on close-packed surfaces of late transition metals. *J. Phys.: Condens. Matter* **2006**, *18*, R481.
(5) Libuda, J.; Freund, H.-J. Molecular beam experiments on model catalysts. *Surf. Sci. Rep.* **2005**, *57*, 157−298.
(6) Jones, F. Teeth and bones: applications of Surface Science to dental Materials and related bioMaterials. *Surf. Sci. Rep.* **2001**, *42*, 75−205.
(7) Roberts, M. Chemisorption and reaction pathways at metal surfaces: the role of surface oxygen. *Chem. Soc. Rev.* **1989**, *18*, 451−475.
(8) Kurahashi, M.; Yamauchi, Y. Steric effect in O_2 sticking on Al(111): Preference for parallel geometry. *Phys. Rev. Lett.* **2013**, *110*, 246102.
(9) Kurahashi, M.; Yamauchi, Y. Spin correlation in O_2 chemisorption on Ni(111). *Phys. Rev. Lett.* **2015**, *114*, 016101.
(10) Kurahashi, M. Oxygen adsorption on surfaces studied by a spin- and alignment-controlled O_2 beam. *Prog. Surf. Sci.* **2016**, *91*, 29−55.
(11) Gerbi, A.; Savio, L.; Vattuone, L.; Pirani, F.; Cappelletti, D.; Rocca, M. Role of Rotational Alignment in Dissociative Chemisorption and Oxidation: O_2 on Bare and CO-Precovered Pd (100). *Angew. Chem., Int. Ed.* **2006**, *45*, 6655−6658.
(12) Vattuone, L.; Gerbi, A.; Cappelletti, D.; Pirani, F.; Gunnella, R.; Savio, L.; Rocca, M. Selective production of reactive and nonreactive oxygen atoms on Pd(001) by rotationally aligned oxygen molecules. *Angew. Chem.* **2009**, *121*, 4939−4942.
(13) Vattuone, L.; Savio, L.; Pirani, F.; Cappelletti, D.; Okada, M.; Rocca, M. Interaction of rotationally aligned and of oriented molecules in gas phase and at surfaces. *Prog. Surf. Sci.* **2010**, *85*, 92−160.
(14) Moritani, K.; Tsuda, M.; Teraoka, Y.; Okada, M.; Yoshigoe, A.; Fukuyama, T.; Kasai, T.; Kasai, H. Effects of Vibrational and Rotational Excitations on the Dissociative Adsorption of O_2 on Cu Surfaces. *J. Phys. Chem. C* **2007**, *111*, 9961−9967.
(15) Wendelken, J. The chemisorption of oxygen on Cu(110) studied by EELS and LEED. *Surf. Sci.* **1981**, *108*, 605−616.
(16) Briner, B.; Doering, M.; Rust, H.-P.; Bradshaw, A. M. Mobility and trapping of molecules during oxygen adsorption on Cu(110). *Phys. Rev. Lett.* **1997**, *78*, 1516.
(17) Prabhakaran, K.; Sen, P.; Rao, C. N. R. Studies of molecular oxygen adsorbed on Cu surfaces. *Surf. Sci.* **1986**, *177*, L971−L977.
(18) Rajumon, M.; Prabhakaran, K.; Rao, C. Adsorption of oxygen on (100), (110) and (111) surfaces of Ag, Cu and Ni: an electron spectroscopic study. *Surf. Sci.* **1990**, *233*, L237−L242.
(19) Liem, S.; Clarke, J.; Kresse, G. Pathways to dissociation of O_2 on Cu (110) surface: first principles simulations. *Surf. Sci.* **2000**, *459*, 104−114.
(20) Liem, S.; Clarke, J.; Kresse, G. Dissociation pathways of oxygen on copper (110) surface: a first principles study. *Comput. Mater. Sci.* **2000**, *17*, 133−140.
(21) Diao, Z. Y.; Han, L. L.; Wang, Z. X.; Dong, C. C. The adsorption and dissociation of O_2 on Cu low-index surfaces. *J. Phys. Chem. B* **2005**, *109*, 5739−5745.
(22) Ge, J.-Y.; Dai, J.; Zhang, J. Z. Dissociative adsorption of O_2 on Cu(110) and Cu(100): Three-dimensional quantum dynamics studies. *J. Phys. Chem.* **1996**, *100*, 11432−11437.
(23) Nesbitt, A.; Lewin, A.; Hodgson, A. Adsorption of oxygen on Cu(110). *J. Phys.: Condens. Matter* **1991**, *3*, S71.
(24) Hodgson, A.; Lewin, A.; Nesbitt, A. Dissociative chemisorption of O_2 on Cu(110). *Surf. Sci.* **1993**, *293*, 211−226.
(25) Ertl, G. Untersuchung von oberflächenreaktionen mittels beugung langsamer elektronen (LEED): I. Wechselwirkung von O_2 und N_2O mit (110)-, (111)- und (100)-Kupfer-Oberflächen. *Surf. Sci.* **1967**, *6*, 208−232.
(26) Jensen, F.; Besenbacher, F.; Laegsgaard, E.; Stensgaard, I. Surface reconstruction of Cu(110) induced by oxygen chemisorption. *Phys. Rev. B* **1990**, *41*, 10233.
(27) Sun, L.; Hohage, M.; Denk, R.; Zeppenfeld, P. Oxygen adsorption on Cu(110) at low temperature. *Phys. Rev. B* **2007**, *76*, 245412.
(28) Döbler, U.; Baberschke, K.; Haase, J.; Puschmann, A. Azimuthal-and Polar-Angle-Dependent Surface Extended X-Ray−Absorption Fine-Structure Study:(2 × 1) O on Cu (110). *Phys. Rev. Lett.* **1984**, *52*, 1437.
(29) Coulman, D. J.; Wintterlin, J.; Behm, R.; Ertl, G. Novel mechanism for the formation of chemisorption phases: The (2 × 1) O-Cu (110) "added row" reconstruction. *Phys. Rev. Lett.* **1990**, *64*, 1761.
(30) Feidenhans, R.; Grey, F.; Nielsen, M.; Besenbacher, F.; Jensen, F.; Laegsgaard, E.; Stensgaard, I.; Jacobsen, K. W.; Nørskov, J. K.; Johnson, R. Oxygen chemisorption on Cu (110): A model for the c(6 × 2) structure. *Phys. Rev. Lett.* **1990**, *65*, 2027.
(31) Liu, W.; Wong, K.; Zeng, H.; Mitchell, K. What determines the structures formed by oxygen at low index surfaces of copper? *Prog. Surf. Sci.* **1995**, *50*, 247−257.
(32) Lian, X.; Xiao, P.; Liu, R.; Henkelman, G. Calculations of the (2 × 1)-O reconstruction kinetics on Cu(110). *J. Chem. Phys.* **2017**, *146*, 111101.
(33) Holloway, S.; Gadzuk, J. Charge transfer, vibrational excitation, and dissociative adsorption in molecule-surface collisions: Classical trajectory theory. *J. Chem. Phys.* **1985**, *82*, 5203−5215.
(34) Diño, W. A.; Kasai, H.; Okiji, A. Orientational effects in dissociative adsorption/associative desorption dynamics of $H_2(D_2)$ on Cu and Pd. *Prog. Surf. Sci.* **2000**, *63*, 63−134.
(35) Kasai, H.; Diño, W. A.; Muhida, R. Surface science-based reaction design: increasing the ortho-para hydrogen conversion yield via molecular orientation, a case study. *Prog. Surf. Sci.* **2003**, *72*, 53−86.
(36) Diño, W. A. Can we probe local surface reactivity with hydrogen molecules? *J. Phys.: Condens. Matter* **2002**, *14*, 4379−4384.
(37) Ertl, G. Reactions at well-defined surfaces. *Surf. Sci.* **1994**, *299−300*, 742−754.
(38) Shimada, I.; Wagner, U. Peruvian Black Pottery Production and Metalworking: A Middle Sicán CraftWorkshop at Huaca Sialupe. *MRS Bull.* **2001**, *26*, 25−30.
(39) Okada, M.; Teraoka, Y. Active oxidation of $Cu_3Au(110)$ using hyperthermal O_2 molecular beam. *Appl. Surf. Sci.* **2010**, *256*, 5676−5680.
(40) Okada, M.; Tsuda, Y.; Oka, K.; Kojima, K.; Diño, W. A.; Yoshigoe, A.; Kasai, H. Experimental and theoretical studies on oxidation of Cu-Au alloy surfaces: effect of bulk Au concentration. *Sci. Rep.* **2016**, *6*, 1−8.
(41) Gerlach, W.; Stern, O. Der experimentelle Nachweis der Richtungsquantelung im Magnetfeld. *Zeitschrift für Physik* **1922**, *9*, 349−352.
(42) Hershbach, D. In *Molecular Beams in Physics and Chemistry: From Otto Sternas Pioneering Exploits to Present-Day Feats*; Friedrich, B., Schmidt-Boecking, H., Eds.; Springer, 2021; pp 1−22.
(43) Tsuda, Y.; Oka, K.; Makino, T.; Okada, M.; Diño, W. A.; Hashinokuchi, M.; Yoshigoe, A.; Teraoka, Y.; Kasai, H. Initial stages of Cu_3Au (111) oxidation: oxygen induced Cu segregation and the protective Au layer profile. *Phys. Chem. Chem. Phys.* **2014**, *16*, 3815−3822.
(44) Trinh, Q. T.; Yang, J.; Lee, J. Y.; Saeys, M. Computational and experimental study of the Volcano behavior of the oxygen reduction activity of PdM@PdPt/C (M = Pt, Ni, Co, Fe, and Cr) core-shell electrocatalysts. *J. Catal.* **2012**, *291*, 26−35.
(45) Moritani, K.; Okada, M.; Sato, S.; Goto, S.; Kasai, T.; Yoshigoe, A.; Teraoka, Y. Photoemission study of the translational energy induced oxidation processes on Cu(111). *Journal of Vacuum Science and Technology. A* **2004**, *22*, 1625−1630.
(46) Over, H.; Gilarowski, G.; Niehus, H. The composition and structure of $Cu_3Au(110)$-(4 × 1): a low-energy electron diffraction analysis. *Surf. Sci.* **1997**, *381*, L619−L622.
(47) Fain, S., Jr; McDavid, J. Work-function variation with alloy composition: Cu-Au. *Phys. Rev. B* **1976**, *13*, 1853.

https://doi.org/10.1021/jacsau.2c00156
JACS Au 2022, 2, 1839−1847

(48) Lide, D. *CRC Handbook of Chemistry and Physics*; CRC Press: Boca Raton, FL, 1998.
(49) Ueta, H.; Kurahashi, M. Dynamics of O_2 Chemisorption on a Flat Platinum Surface Probed by an Alignment-Controlled O_2 Beam. *Angew. Chem., Int. Ed.* **2017**, *56*, 4174−4177.
(50) Citri, O.; Baer, R.; Kosloff, R. The role of non adiabatic mechanisms in the dissociation dynamics of O_2 on silver surfaces. *Surf. Sci.* **1996**, *351*, 24−42.
(51) Katz, G.; Zeiri, Y.; Kosloff, R. Nonadiabatic charge transfer processes of oxygen on metal surfaces. *Isr. J. Chem.* **2005**, *45*, 27−36.
(52) Kohn, W.; Sham, L. J. Self-consistent equations including exchange and correlation effects. *Phys. Rev.* **1965**, *140*, A1133.
(53) Hohenberg, P.; Kohn, W. Inhomogeneous electron gas. *Phys. Rev.* **1964**, *136*, B864.
(54) Kresse, G.; Furthmüller, J. Efficiency of ab-initio total energy calculations for metals and semiconductors using a plane-wave basis set. *Comput. Mater. Sci.* **1996**, *6*, 15−50.
(55) Kresse, G.; Furthmüller, J. Efficient iterative schemes for ab initio total-energy calculations using a plane-wave basis set. *Phys. Rev. B* **1996**, *54*, 11169.
(56) Kresse, G.; Hafner, J. Ab initio simulation of the metal/nonmetal transition in expanded fluid mercury. *Phys. Rev. B* **1997**, *55*, 7539.
(57) Kresse, G.; Hafner, J. Ab initio molecular-dynamics simulation of the liquid-metal-amorphous-semiconductor transition in germanium. *Phys. Rev. B* **1994**, *49*, 14251.
(58) Kresse, G.; Joubert, D. From ultrasoft pseudopotentials to the projector augmented-wave method. *Phys. Rev. B* **1999**, *59*, 1758.
(59) Perdew, J. P.; Chevary, J. A.; Vosko, S. H.; Jackson, K. A.; Pederson, M. R.; Singh, D. J.; Fiolhais, C. Atoms molecules, solids, and surfaces: Applications of the generalized gradient approximation for exchange and correlation. *Phys. Rev. B* **1992**, *46*, 6671.
(60) Perdew, J. P.; Burke, K.; Ernzerhof, M. Generalized gradient approximation made simple. *Phys. Rev. Lett.* **1996**, *77*, 3865.
(61) Monkhorst, H. J.; Pack, J. D. Special points for Brillouin-zone integrations. *Phys. Rev. B* **1976**, *13*, 5188.
(62) Tang, W.; Sanville, E.; Henkelman, G. A grid-based Bader analysis algorithm without lattice bias. *J. Phys.: Condens. Matter* **2009**, *21*, 084204.
(63) Sanville, E.; Kenny, S. D.; Smith, R.; Henkelman, G. Improved grid-based algorithm for Bader charge allocation. *J. Comput. Chem.* **2007**, *28*, 899−908.
(64) Henkelman, G.; Arnaldsson, A.; Jónsson, H. A fast and robust algorithm for Bader decomposition of charge density. *Comput. Mater. Sci.* **2006**, *36*, 354−360.
(65) Yu, M.; Trinkle, D. R. Accurate and efficient algorithm for Bader charge integration. *J. Chem. Phys.* **2011**, *134*, 064111.
(66) Momma, K.; Izumi, F. VESTA3 for three-dimensional visualization of crystal, volumetric and morphology data. *J. Appl. Crystallogr.* **2011**, *44*, 1272−1276.

https://doi.org/10.1021/jacsau.2c00156
JACS Au 2022, 2, 1839−1847